JOURNAL OF GEOPHYSICAL RESEARCH: SPACE PHYSICS, VOL. 118, 4711–4723, doi:10.1002/jgra.50444, 2013

Understanding shock dynamics in the inner heliosphere with modeling and type II radio data: A statistical study

H. Xie,[1,2] O. C. St. Cyr,[2] N. Gopalswamy,[2] D. Odstrcil,[3] and H. Cremades[4]

Received 4 March 2013; revised 29 May 2013; accepted 6 July 2013; published 1 August 2013.

[1] We study two methods of predicting interplanetary shock location and strength in the inner heliosphere: (1) the ENLIL simulation and (2) the kilometric type II (kmTII) prediction. To evaluate differences in the performance of the first method, we apply two sets of coronal mass ejections (CME) parameters from the cone-model fitting and flux-rope (FR) model fitting as input to the ENLIL model for 16 halo CMEs. The results show that the ENLIL model using the actual CME speeds from FR-fit provided an improved shock arrival time (SAT) prediction. The mean prediction errors for the FR and cone-model inputs are 4.90 ± 5.92 h and 5.48 ± 6.11 h, respectively. A deviation of 100 km s^{-1} from the actual CME speed has resulted in a SAT error of 3.46 h on average. The simulations show that the shock dynamics in the inner heliosphere agrees with the drag-based model. The shock acceleration can be divided as two phases: a faster deceleration phase within 50 R_S and a slower deceleration phase at distances beyond 50 R_S. The linear-fit deceleration in phase 1 is about 1 order of magnitude larger than that in phase 2. When applying the kmTII method to 14 DH-km CMEs, we found that combining the kmTII method with the ENLIL outputs improved the kmTII prediction. Due to a better modeling of plasma density upstream of shocks and the kmTII location, we are able to provide a more accurate shock time-distance and speed profiles. The mean kmTII prediction error using the ENLIL model density is 6.7 ± 6.4 h; it is 8.4 ± 10.4 h when the average solar wind plasma density is used. Applying the ENLIL density has reduced the mean kmTII prediction error by ∼2 h and the standard deviation by 4.0 h. Especially when we applied the combined approach to two interacting events, the kmTII prediction error was drastically reduced from 29.6 h to –4.9 h in one case and 10.6 h to 4.2 h in the other. Furthermore, the results derived from the kmTII method and the ENLIL simulation, together with white-light data, provide a valuable validation of shock formation location and strength. Such information has important implications for solar energetic particle acceleration.

Citation: Xie, H., O. C. St. Cyr, N. Gopalswamy, D. Odstrcil, and H. Cremades (2013), Understanding shock dynamics in the inner heliosphere with modeling and type II radio data: A statistical study, *J. Geophys. Res. Space Physics*, *118*, 4711–4723, doi:10.1002/jgra.50444.

1. Introduction

[2] Interplanetary (IP) shocks driven by coronal mass ejections (CMEs) can have profound effects on the Earth's space weather environment. In particular, the CME-driven shocks can accelerate solar energetic particles (SEPs) efficiently [e.g., *Mewaldt*, 2006] and cause severe geomagnetic storms when the shock sheath and/or the driving IP CME (ICME) contains southward magnetic field [e.g., *Tsurutani et al*., 1988]. When a shock travels outward from the solar corona, it can accelerate electrons that produce type II radio emission at the local plasma frequency or its harmonic. These radio emissions can start at frequencies ∼250 MHz in the low corona and extend all the way to 1 AU, where the local plasma frequency of the solar wind is ∼25 kHz [*Gopalswamy et al.*, 2005a]. Low-frequency radio bursts at the decameter-hectometric (DH) (1–14 MHz) and kilometric (km) (< 300 kHz) domains are of particular interest because they are produced when the CME/shocks leave the outer corona (coronagraph field of view) and propagate into the IP medium. Combined white-light and radio observations provide important diagnostics for the CME/shock and the ambient solar wind medium.

[3] Recently, *Xie et al.* [2012] conducted a case study of the 3 April 2010 CME/shock propagation combining

[1]Department of Physics, Catholic University of America, Washington, DC, USA.
[2]NASA Goddard Space Flight Center, Greenbelt, Maryland, USA.
[3]Department of Computational and Data Sciences, George Mason University, Fairfax, Virginia, USA.
[4]UTN-FRM/CONICET, Mendoza, Argentina.

Corresponding author: H. Xie, Department of Physics, Catholic University of America, 200 Hannan Hall, Washington, DC 20064, USA. (hong.xie@nasa.gov)

2169-9380/13/10.1002/jgra.50444

the Solar Terrestrial Relations Observatory (STEREO), the Solar and Heliospheric Observatory (SOHO) white-light observations, and type II radio data with numerical simulations. They compared two methods of predicting shock arrival time. The first method is a heliospheric Wang-Sheeley-Arge (WSA)-Cone-ENLIL simulation model (shortened as ENLIL hereafter), which is a three-dimensional (3-D) MHD model combined with the Wang-Sheeley-Arge (WSA) coronal maps and the CME observations [*Odstrcil et al.*, 2004; *Odstrcil et al.*, 2005; *Odstrcil and Pizzo*, 2009]. The second method is a technique based on the kilometric type II radio emissions described by *Cremades et al.* [2007] (hereafter called kmTII technique). The results showed that the ENLIL model predicted well not only the kinematics of shock propagation but also reproduced most large-scale ambient solar wind and shock structures. The shock time-distance profiles derived from the ENLIL model agreed well with those measurements in the J-maps along the CME leading edge and the Sun-Earth line. The fitted deceleration of shock propagation from the ENLIL outputs was consistent with that inferred from the J-map, as well as that obtained from *Gopalswamy et al.*'s [2005b] empirical shock arrival model. The kmTII prediction relies largely on the plasma density n_0 at 1 AU, which is assumed to be the average solar wind value of 7.2 cm^{-3} in *Cremades et al.* [2007]. Using the ENLIL model density, *Xie et al.* [2012] found that the kmTII prediction error was reduced from 15 h to 2 h for the 3 April 2010 event.

[4] In this paper, we extend the previous work of *Xie et al.* [2012] and apply the two methods to a subset of halo CMEs [*Gopalswamy et al.*, 2010] (http://cdaw.gsfc.nasa.gov/CME_list/halo/halo.html). We first use the ENLIL model simulation to study 16 halo CME events during solar cycle 24. Two sets of CME fitting inputs derived from (1) single-perspective cone model [*Xie et al.*, 2004] and (2) multiperspective graduated-cylindrical-shell (GCS) flux-rope forward modeling [*Thernisien et al.*, 2006] are used in the simulation to evaluate how the model performance depends on the CME inputs. We then apply the kmTII method to a subset of CMEs that are associated with both the DH and km type II bursts (DH-km CMEs). We combine the kmTII technique with the ENLIL simulations to study the effects of solar wind plasma density and CME interactions on the kmTII prediction.

[5] The main purpose of the paper is to report a statistical analysis that studies two methods to determine (1) how the shock dynamics and shock arrival time depend on the CME input speed in the ENLIL simulation and (2)whether or not a combination of techniques yields a better prediction. The rest of the paper is organized as follows. Section 2 describes the WSA-Cone-ENLIL model, data and CME fitting, and simulation results. Section 3 introduces the kmTII technique, data selection, and how to improve the kmTII prediction using the ENLIL simulation results. Section 4 gives the discussion. Finally, conclusions are presented in section 5.

2. Simulation With the WSA-Cone-ENLIL Model

2.1. Numerical Model

[6] The WSA-Cone-ENLIL model is well known in the solar and heliospheric community, and ENLIL version 2.3a is currently available to users at the Community Coordinated Modeling Center (CCMC). ENLIL is a time-dependent 3-D MHD model of the heliosphere, and it solves for plasma mass, momentum, and energy density, as well as magnetic field, using a Total-Variation-Diminishing Lax-Friedrich (TVDLF) algorithm [*Toth and Odstrcil*, 1996]. In the simulation, spherical coordinates are used, and the three independent spatial variables are the radial position r, the meridional (latitude) angle θ, and the azimuthal (longitude) angle ϕ. The meridional and azimuthal extents span 30°–150° and 0°–360°, respectively. The computational region has $256 \times 30 \times 90$ grid points, and the uniform spacing of computational grid points are $\Delta r = 1.588\ R_s$, $\Delta\theta = 4°$, and $\Delta\phi = 4°$.

[7] The simulation is done in two stages: (1) set up the background solar wind based on the Wang-Sheeley-Arge (WSA) [e.g., *Arge and Pizzo*, 2000; *Arge et al.*, 2004] model; (2) insert a hydrodynamic spherical ejecta propagating in that background at the time when the observed CME passes the inner boundary at 21.5 R_s. The inserted ejecta has a uniform velocity and diameter corresponding to the fitted radial CME speed and angular width. In addition, the simulation assumes that the ejecta has a density four times larger than the mean value in the fast stream and the same temperature as in the fast stream. The background solar wind was set up using the WSA model with photospheric magnetograms from the National Solar Observatory's (NSO) Global Oscillation Network Group (GONG) system. A constant momentum flow and thermal pressure are assumed at the boundary. The density, temperature, and flow speed in the fast stream are set to be 300 cm^{-3}, 0.8 MK, and 625 km s^{-1}, respectively.

2.2. Data and CME Fitting

[8] The Sun Earth Connection Coronal and Heliospheric Investigation (SECCHI) on board STEREO [*Kaiser et al.*, 2008] and the Large Angle and Spectrometric Coronagraph Experiment (LASCO; *Brueckner et al.* [1995]) on board SOHO [*Domingo et al.*, 1995] together provide a wealth of multiviewpoint CME observations during solar cycle 24. A large number of CMEs have been observed by STEREO (http://cor1.gsfc.nasa.gov/catalog/) and SOHO (http://cdaw.gsfc.nasa.gov/CME_list/). Table 1 lists 16 halo CMEs in the rising phase of cycle 24 (till the end of March 2012). The CMEs in this study were selected based on the following criteria: (1) they are Earth-directed halo CMEs in LASCO and originate from near central meridian within ± 45° longitude and (2) the associated IP shocks have been detected near Earth by either the Wind and/or the Advanced Composition Explorer (ACE) spacecraft.

[9] To identify the IP shocks, we first chose the IP shock candidates from two automated shock lists: (1) the SOHO proton monitor shocks (http://umtof.umd.edu/pm) and (2) ACE real-time shocks (http://www.srl.caltech.edu/ACE/ASC/DATA/Shocks/). We then used the Shock and Discontinuities Analysis Tool (SDAT) [*Viñas and Holland*, 2005] to verify the shocks and determine the shock parameters. SDAT uses an extension of the *Viñas and Scudder* [1986] analysis method, which is based on the Rankine-Hugoniot conservation equations, to derive shock parameters such as the shock speed, Mach number, normal components, and angle between the normal and the magnetic field. SDAT can be applied to any satellite observations of plasma and

Table 1. Summary of the Properties of the 16 Halo CME/Shocks and the ENLIL Predictions[a]

CME			FR-Fit		Cone-Fit		IP Shock		
Date (UT)	Vsky ($km\,s^{-1}$)	Loc_sc	V_{FR} ($km\,s^{-1}$)	ω_{broad} (deg)	V_{cone} ($km\,s^{-1}$)	ω_{cone} (deg)	Date (UT)	Err-FR (h)	Err-Cone (h)
2010/02/07 03:54	429	N21E11	525	39	580	52	2010/02/11 00:00	–14.29	–18.20
2010/02/12 13:42	509	N21E07	752	38	791	40	2010/02/15 17:39	–6.50	–6.32
2010/04/03 10:34	668	S25W03	1011	37	914	41	2010/04/05 07:58	0.73	6.87
2010/05/24 14:06	474	S15W18	650	38	611	48	2010/05/28 01:53	–13.01	–8.25
2011/02/15 02:24	471	S21W18	651	41	624	49	2011/02/18 00:48	–6.94	–4.90
2011/06/21 03:16	719	N16W08	1031	36	1211	39	2011/06/23 02:31	6.71	2.21
2011/07/09 00:48	747	S17E20	751	39	922	39	2011/07/11 08:27	–1.84	–5.75
2011/08/04 04:12	1315	N19W36	1722	50	1556	47	2011/08/05 18:41	0.08	–1.81
2011/09/06 23:05	575	N14W18	1033	45	832	39	2011/09/09 11:47	–5.96	0.45
2011/10/27 12:00	570	N33E15	716	47	821	32	2011/10/30 08:41	1.36	3.56
2011/11/09 13:36	1076	N24E35	1288	38	1239	44	2011/11/12 05:10	–3.02	–6.81
2012/01/19 14:36	1272	N33E27	1327	40	1494	48	2012/01/22 05:33	–4.10	–6.55
2012/01/23 04:00	2102	N33W21	2002	50	2456	53	2012/01/24 14:38	4.97	–2.57
2012/03/07 00:24	2405	N17E27	2349	40	2950	49	2012/03/08 10:30	3.78	–5.08
2012/03/09 04:26	863	N17W03	1281	43	1168	53	2012/03/11 12:30	–4.48	–3.23
2012/03/10 18:12	1037	N17W24	1705	44	1378	49	2012/03/12 08:30	0.60	5.17

[a]Columns 1–3: CME date and first appearance time on C2, sky-plane speed, and solar source location; columns 4 and 5: flux-rope model-fit radial speed and face-on half width; columns 6 and 7: cone-model-fit radial speed and half width; column 8: IP shock date and time at Wind; columns 9 and 10: ENLIL prediction errors using FR-fit and cone-fit inputs. Note that the listed V_{FR} and V_{cone} are the CME speeds at 21.5 R_s after they decelerated or accelerated through the corona. Dates are formatted as year/month/day.

magnetic field data (a summary of the derived shock parameters is available in http://cdaw.gsfc.nasa.gov/pub/hong/sdat-shockpara.txt). Figure 1 shows an example of the shock analysis using SDAT for the 23 January 2012 event. In the analysis, we used the 92 s plasma data from the Wind Solar Wind Experiment (SWE) and the 1 min magnetic field data from the Wind Magnetic Fields Investigation (MFI). The obtained shock speed, Alfvén Mach number, and angle between the normal and the magnetic field are 646.6 ± 17.3 km/s, 3.4, and 56°, respectively. The shock arrived at Wind at ~14:38 UT on 24 January, and the CME erupted from the Sun at ~03:38 UT on 23 January, which yields the shock transit speed of ~1183 km/s, indicating that the shock had decelerated during its propagation from the Sun to the Earth (see details in Figure 5c).

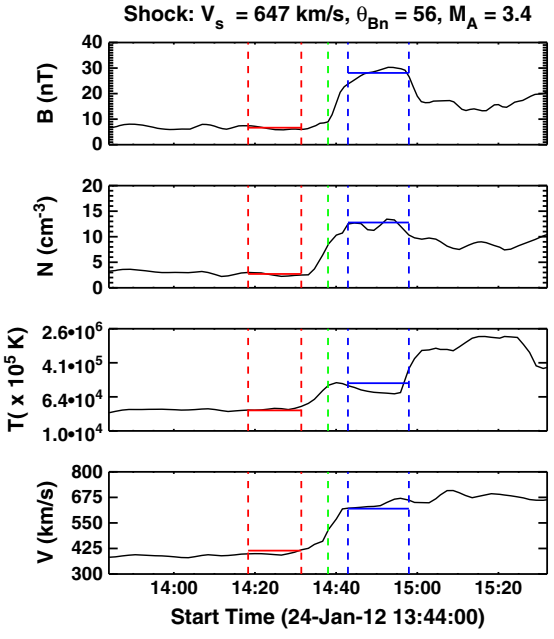

Figure 1. An example of the shock analysis for the 23 January 2012 event. Black solid curves represent Wind magnetic field and plasma observational data. Red and blue horizontal lines mark the values of each parameter that derived from the model-fit process. Green dash vertical line indicates the shock time. Red and blue dash vertical lines denote selected analysis intervals upstream and downstream of the shock.

[10] To match the associated IP shock and the CME, we examine all the halo CMEs detected by SOHO/ LASCO over an interval of 1–5 days preceding the shock arrival and choose the best candidate that occurs on the front side of the Sun and is compatible with the observed in situ speed, similar to the previous study [*Gopalswamy*, 2011]. Table 1 lists the CME date and time, sky-plane speed, associated flare location, flux-rope model-fit velocity and face-on half width, cone-model-fit velocity and half width, IP shock date and time, and the ENLIL prediction error with flux-rope model fit and cone-model fit inputs.

2.3. CME Fitting

[11] Two CME models, (1) Xie-Ofman-Lawrence (XOL) cone model [*Xie et al.*, 2004] and (2) graduated-cylindrical-shell (GCS) flux-rope (FR) model [*Thernisien et al.*, 2006], were used independently to obtain the CME radial speed, angular width, and propagation direction, which are fed into the ENLIL code.

[12] Figure 2 shows an example of the CME fitting for the 23 January 2012 event. The 23 January 2012 CME originated from NOAA Active Region (AR) 11402 N33W21 at ~03:38 UT. SOHO observed a halo CME at ~04:00 UT, and STEREO A and B observed an east (~ 88°E) and west (~ 135°W) limb CME at ~03:45 UT. The flux-rope fitting (FR-fit) gave the CME radial speed V_{FR} = 2002 $km\,s^{-1}$, and

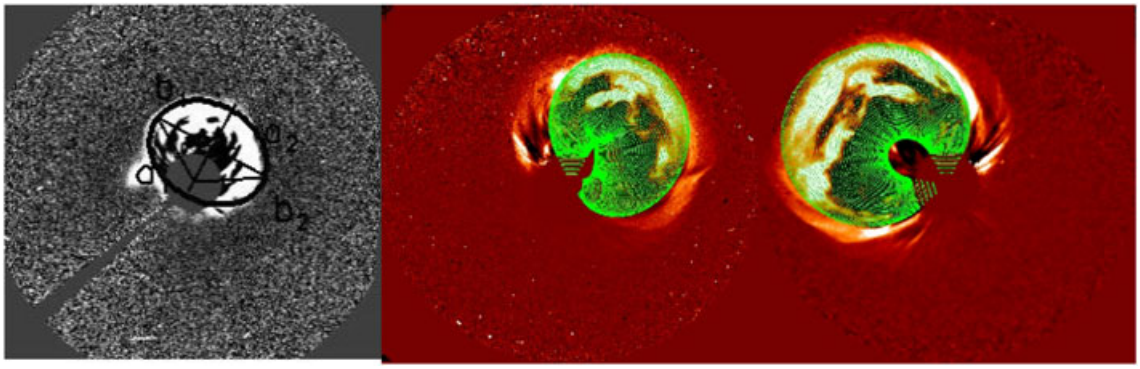

Figure 2. An example of the CME fitting for the 23 January 2012 event. (left) Cone-model fitting superimposed with C3 image at 04:54 UT; COR2 images on (middle) STEREO B and (right) STEREO A at 04:54 UT with the FR projected wireframe (green curves) overlaid on top.

the half angular widths from face-on and edge-on views ω_{broad} = 50° and ω_{edge} = 43°. The cone model assumes that ω_{broad} = ω_{edge}, yielding the CME radial speed V_{cone} = 2495 km s^{-1} and the half width ω_{half} = 53°. The discrepancy of the CME radial speeds from the two models is 493 km s^{-1}. The face-on half width from the FR-fit is similar to the cone half width.

[13] Figure 3 compares the two CME model-fit speeds for the 16 CMEs. It is shown that the mean cone-fit CME speed (1204 km s^{-1}) is slightly larger than the mean FR-fit speed (1159 km s^{-1}). The maximum difference between the two sets of model-fit speeds is 601 km s^{-1}. There is no significant difference between the FR-fit face-on half width and the cone-fit half width. The difference between the mean values of these two half widths is 5° with a maximum of 13°.

2.4. WSA-Cone-ENLIL Results

[14] To study the effect of the CME inputs on the ENLIL model, we applied the two sets of inputs in the simulations for the 16 CMEs: (1) the FR-fit speed and face-on half width and (2) the cone-fit speed and half width. Figure 4 shows an example of the simulated two-dimensional (2-D) density contour in the ecliptic plane (left), meridian plane (middle), and at R = 1 AU surface (right) on 23 January 2012 at 18:00 UT (movies are available online: http://ccmc.gsfc.nasa.gov/database_SH/Hong_Xie_041212_SH_3.php). The density in the simulation is normalized for an r^2 falloff with distance. The heliographic location of the Earth is S5.3W00, marked by yellow filled circles in the figure. The CME leading edge (LE) is along the N33W21 direction. Figure 5a shows 1-D density profile along the Sun-Earth line at 10:01:27 on 23 January using the FR-fit input, where the radial positions of the shock front, upstream, and downstream are marked by three vertical lines r_{shk}, r_{up}, and r_{dw}, and the shock location is defined as where the largest density jump occurs, as in *Xie et al.* [2012]. Figure 5b shows the shock time-distance profiles along the LE and Sun-Earth directions. V_{fit-LE} and $V_{fit-Ear}$ are the linear-fit velocities from the simulation along the two directions. Figure 5c plots the shock time-velocity profiles showing that the shock had undergone a deceleration with a_{fit-LE} = –4.46 m/s^2 and $a_{fit-Ear}$ = –5.02 m/s^2, and a_{fit-LE} and $a_{fit-Ear}$ are the linear-fit accelerations along the LE and Sun-Earth directions, respectively. The ENLIL prediction error in Figure 5b is computed as $Err_{enlil} = T_{enlil} - T_{obs}$, where T_{enlil} and T_{obs} are the ENLIL and Wind shock arrival times (SAT). For the 23 January 2012 event, the ENLIL model SAT at Earth is 19:37 UT on 24 January, yielding a prediction error of ~5.0 h compared to the Wind SAT of 14:38 UT [*Joshi et al.*, 2013]. The ENLIL shock speed at 1 AU is 722 km/s in Figure 5c, which is comparable to the Wind shock speed of 647 km/s, with an error of ~75 km/s.

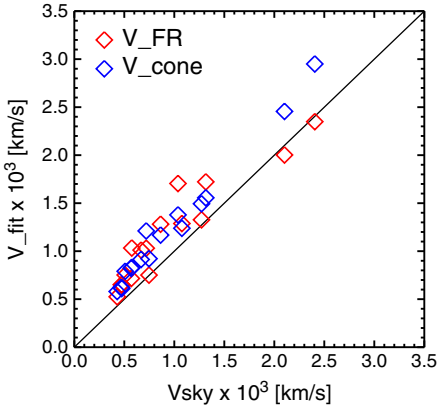

Figure 3. Comparison of the CME radial speeds from the two model inputs for all 16 CMEs: the FR-fit speed V_{FR} (red diamond) and cone-fit speed V_{cone} (blue diamond) versus the sky-plane speed V_{sky}. Overplotted solid line denotes the line where the fit speed V_{fit} = V_{sky}.

[15] Figure 6a plots the ENLIL prediction errors using FR-fit inputs (red diamonds) and cone-fit inputs (blue diamonds) versus the sky-plane speeds of the 16 CMEs. In general, the absolute values of the prediction errors using cone-fit inputs, Err_c, are larger than those using FR-fit inputs, Err_F. The mean of the absolute values of the prediction errors for the FR and cone model are 4.90 h and 5.48 h, respectively. The standard deviations of the prediction errors for the two sets of inputs are ±5.92 and ±6.11, indicating the scattering of the SAT prediction error is relatively small for both inputs. Using the FR-fit speed has improved the mean SAT prediction error by ~0.58 h and the standard deviation

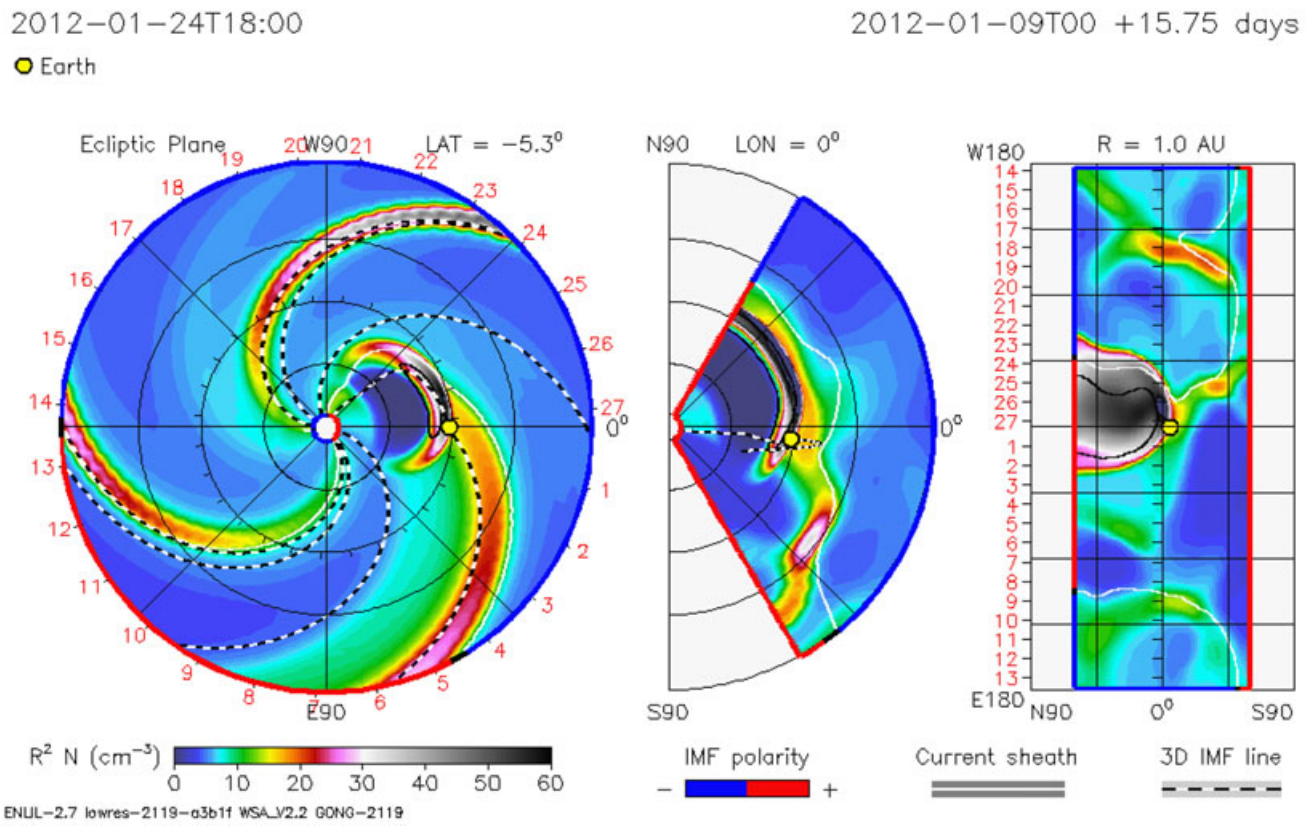

Figure 4. Simulated 2-D density contours in the (left) ecliptic plane, (middle) meridian plane, and (right) R = 1 AU surface on 24 January 2012, 18:00 UT. The density in the simulation is normalized for an r^{-2} falloff with distance.

by 0.19 h. Figure 6b plots the difference of the prediction errors, $\Delta_{\mathrm{Err}} = |\mathrm{Err}_F - \mathrm{Err}_c|$, versus the difference of input speeds, $\Delta_{\mathrm{Vfit}} = |V_{\mathrm{FR}} - V_{\mathrm{cone}}|$. The linear fit gives $\Delta_{\mathrm{Err}} = 2.17 + 0.01\Delta_{\mathrm{Vfit}}$ with a correlation coefficient (CC) of 0.72. A variation in the CME input speed of 100 km/s results in a difference of 3.46 h in the model prediction error on average (see detailed discussion in section 4).

3. The kmTII Prediction

3.1. Data Selection

[16] The data set in the kmTII study were selected based on two criteria: (1) the CMEs are associated with type II bursts in the DH-km wavelength domain with high frequency extending to ≥ 5000 kHz and low frequency to

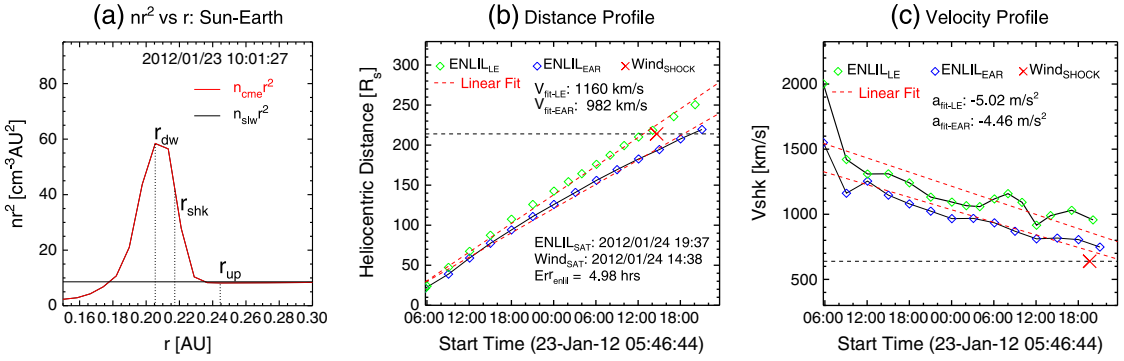

Figure 5. (a) One-dimensional density profile along the Sun-Earth line: nr^2 (density times square of radial distance) versus distance r, where red and black lines denote the CME and ambient solar wind plasma density, respectively. (b) Time-distance profile of the shock along the LE direction and Sun-Earth line direction for the 23 January 2012 CME, where the dashed line denotes linear-fit distance and the Wind shock time is marked by the red cross. (c) Time-velocity profile of the shock along the LE direction and Sun-Earth line direction for the 23 January 2012 CME, where the dashed line denotes linear-fit velocity and the Wind shock speed is marked by the red cross.

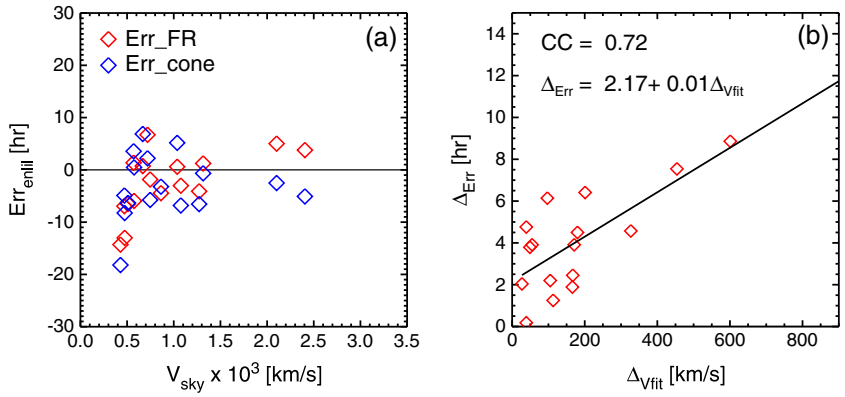

Figure 6. (a) Prediction errors versus CME sky-plane speed for all 16 CMEs. Red and blue diamonds denote the prediction errors using the FR-fit and cone-fit inputs, respectively. (b) Difference of prediction errors Δ_{Err} as function of input speed difference Δ_{Vfit}, where $\Delta_{\mathrm{Err}} = |\mathrm{Err}_F - \mathrm{Err}_c|$ and $\Delta_{\mathrm{Vfit}} = |V_{\mathrm{FR}} - V_{\mathrm{cone}}|$.

$\leq$ 400 kHz components; (2) the CMEs are associated with IP shocks detected by either Wind, ACE, or STEREO A and B. We chose DH-km CMEs because the DH type II burst is produced by the CME/shock near the Sun whose onset is closely correlated to the CME onset. Thus, we can match unambiguously the type II bursts with the CME/shock events [*Gopalswamy et al.*, 2001a; *Gopalswamy et al.*, 2005a]. Note that also to enlarge the analysis data set, we used 400 kHz (instead of 300 kHz) for the kmTII frequency limit.

[17] There are 18 DH-km CMEs during the rising phase of cycle 24 (until the end of March 2012) in the preliminary list of the Wind Radio and Plasma Wave (WAVES) experiment [*Bougeret et al.*, 1995] (http://ssed.gsfc.nasa.gov/waves/data_products.html). CMEs and flares associated with the type II bursts are also listed in the online catalog (http://cdaw.gsfc.nasa.gov/CME_list/radio/waves_type2.html). After eliminating four events that had no corresponding IP shocks, we end up with a list of 14 DH-km CMEs. Table 2 lists the 14 DH-km CMEs with the CME date, shock-observing spacecraft, associated flare location with respect to the shock-observing spacecraft, FR-fit velocity, face-on half width, IP shock arrival, ENLIL prediction error, kmTII prediction errors, ENLIL model density, sampled kmTII frequency range, kmTII prediction uncertainty, and associated SEP intensity. DH-km CMEs are generally more energetic, and majority of them are associated with SEP events [*Gopalswamy et al.*, 2005a]. In this study, 12 of the 14 DH-km CMEs were associated with SEP events. Eight of these events are common with the study present in section 2.

3.2. The kmTII Method

[18] Using a simple density model in which $n = n_0/r^2$ (n_0 is the plasma density at 1 AU in units of cm^{-3}) [e.g., *Leblanc et al.*, 1998], the time-distance profile of the CME-driven shock can be derived from the frequency drift given by

$$r(t) = a\sqrt{n_0}/f(t), \tag{1}$$

where $r(t)$ is the heliocentric distance where the kmTII occurs in units of AU, $f(t)$ is the drifting frequency in units of kHz, and a = 9 or 18 is a constant for fundamental or

Table 2. Summary of the Properties of the 14 DH-km CME/Shocks, ENLIL, and kmTII Predictions[a]

CME			FR-fit		IP Shock		$\mathrm{Err}_{\mathrm{kmTII}}$					SEP
Date (UT)	SC	Loc	V_{FR} (km/s)	ω_{bd} (deg)	Date (UT)	$\mathrm{Err}_{\mathrm{EN}}$ (h)	km_1 (h)	km_2 (h)	$n_{0\mathrm{enlil}}$ (cm^{-3})	f-Range (kHz)	UTN (h)	Int (pfu)
2011/02/15 02:24	S	S21W18	651	41	02/18 00:48	–6.9	–2.8	17.5	12.0	928–339	± 14	3
2011/08/04 04:12	S	N19W36	1722	50	08/05 18:41	0.1	–6.7	–1.3	9.8	478–268	± 8	96
2011/09/06 23:05	S	N14W18	1033	45	09/09 11:47	–6.0	–4.9	29.6	17.7	500–268	± 12	9
2011/11/09 13:36	S	N26E43	1288	38	11/12 05:10	–3.0	–15.5	–3.4	12.4	930–490	± 13	n/a
2012/01/19 14:36	S	N33E27	1327	40	01/22 05:33	–4.1	–13.2	–6.6	9.1	478–199	± 13	4
2012/01/23 04:00	S	N33W21	2002	50	01/24 14:38	5.0	–1.7	4.0	9.7	400–140	± 7	3000
2012/03/07 00:24	S	N17E27	2349	40	03/08 10:30	3.8	1.5	14.2	12.8	292–163	± 7	1500
2012/03/10 18:12	S	N17W24	1705	44	03/12 08:30	0.6	–9.0	–2.7	10.5	450–108	± 8	1490
2011/03/07 20:00	A	N31E34	2283	57	03/09 06:47	–11.3	4.2	10.6	16.5	380–154	± 16	50
2011/06/07 06:49	A	S21E40	1525	42	06/09 22:40	–14.4	1.0	2.9	7.6	768–249	± 13	73
2011/09/22 10:48	B	N09W07	1818	56	09/24 03:58	–10.5	–9.1	4.4	13.8	391–192	± 8	35
2012/01/27 18:27	A	N27E36	2658	55	01/29 13:04	–8.3	–9.6	–1.7	10.7	374–158	± 8	796
2012/03/13 17:36	A	N17E43	2182	49	03/15 22:32	–5.9	–11.3	–4.6	10.4	699–328	± 11	469
2012/03/18 00:24	A	N19E09	1279	57	03/19 19:17	3.9	4.5	14.6	10.4	202–110	± 9	n/a

[a]Columns 1–3: CME date and first appearance time on C2, shock-observing spacecraft (S: SOHO, A: STEREO A, B: STEREO B), and solar source location with respect to the shock-observing spacecraft; columns 4 and 5: FR-fit radial speed and face-on half width; column 6: IP shock date and time at Wind; column 7: ENLIL prediction error; columns 8 and 9: kmTII prediction errors using $n_{0\mathrm{enlil}}$ and $n_{0\mathrm{avg}}$; columns 10–12: ENLIL model density, sampled frequency range, and kmTII prediction uncertainty; column 13: SEP intensity, pfu = proton flux units = particles/[sr·cm^2·s]. Dates are formatted as year/month/day and month/day where applicable.

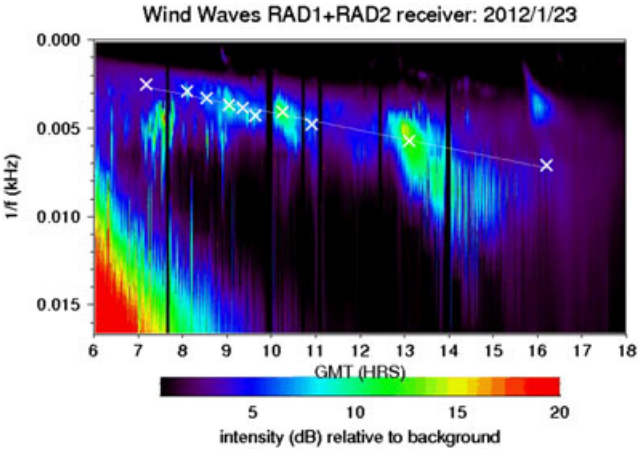

Figure 7. The kmTII dynamic spectrum detected by Wind/WAVEs on 23 January 2012. White cross symbols denote the sampled data points. Note that the herringbone structure that occurred around 13:00–15:00 UT was excluded from the sampled data.

harmonic emission, respectively. The derived shock speed is given by

$$V_{sh} = a\sqrt{n_0} \times \frac{d}{dt}(1/f) \times 1.5 \times 10^8, \quad (2)$$

where the V_{sh} is the kmTII shock speed (km s^{-1}) and $\frac{d}{dt}(1/f)$ is the slope of drifting $1/f$ (kHz) [*Reiner et al.*, 1998]. This is valid only in the kilometer range because the density variation is not r^{-2} for DH domain [*Gopalswamy*, 2011]. Figure 7 shows a type II dynamic spectrum detected by Wind/WAVES on 23 January 2012. The kmTII started from ~07:00 UT to 13:00 UT with a frequency range of ~400 kHz to 100 kHz. Note that in the figure the scale of the vertical axis is in units of $1/f$. The solid line is the linear fit of the drifting $1/f$ as a function of time. White cross symbols denote sampled data points along the kmTII emission from which we infer the shock distance and speed. Note that we have excluded the herringbone structure that occurred around 13:00–15:00 UT in the kmTII burst.

3.3. Improved kmTII Predictions Using the ENLIL Simulation Results

3.3.1. Effect of Upstream Solar Wind Density on the kmTII Prediction

[19] The kmTII prediction relies on the coronal density model and the electron density n_0 at 1 AU, which is assumed to be the average solar wind value of 7.2 cm^{-3} [*Cremades et al.*, 2007]. To improve the prediction, we apply the plasma density obtained from the ENLIL simulation in equations (1) and (2) for the 14 DH-km CMEs. Figure 8 shows 2-D density contours at $r = r_{up}$ surface for three events: (a) the 23 January 2012 event and two interacting cases of (b) the 6 September 2011 event, and (c) the 7 March 2011 event. In the figure, r_{up} denotes the radial distance upstream of the shock and black circle defines the half angular width of the CME/shock. Cross and triangular symbols mark the locations of the CME/shock leading edges (LEs) and the maximum density within the shock front.

[20] Taking the 23 January 2012 event as an example, the ENLIL simulation gave the kmTII plasma density n_{0enlil} = 9.7 cm^{-3}, assuming that the kmTII occurs near the shock LE at 0.22 AU. The modeled 2-D density contour shows that the CME/shock had encountered a streamer belt and the plasma density upstream of the shock varied from 9.7 cm^{-3} to 14.2 cm^{-3}, resulting in a bandwidth-to-frequency ratio (BFR) [*Aguilar-Rodriguez et al.*, 2005] $|df/f| = \sim 20\%$. This result agrees well with the spectrum observation, as shown in Figure 7. Figure 9 (right) plots the time-distance profile of the shock propagation inferred from the kmTII data, superimposed with shock trajectories extracted from the ENLIL model (red circles) and the FR-fit to the CME/shock images (blue squares) from Heliospheric Imager (HI1) [*Eyles et al.*, 2009]. Note that all the distances above are measured along the CME/shock LE direction. In the figure, kmTII$_1$ (green) and kmTII$_2$ (magenta) denote the shock distances corresponding to n_{0enlil} and n_{0avg},

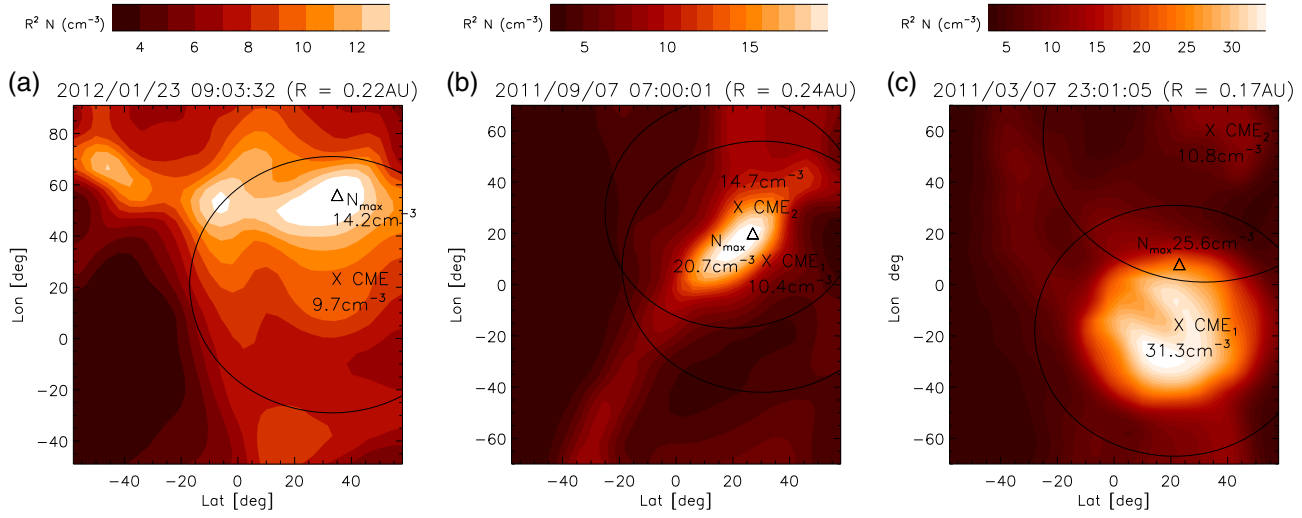

Figure 8. Simulated 2-D density contours at $r = r_{up}$ surface showing the normalized plasma density upstream of the CME/shocks on (a) 23 January 2012, (b) 7 September 2011, and (c) 7 March 2011.

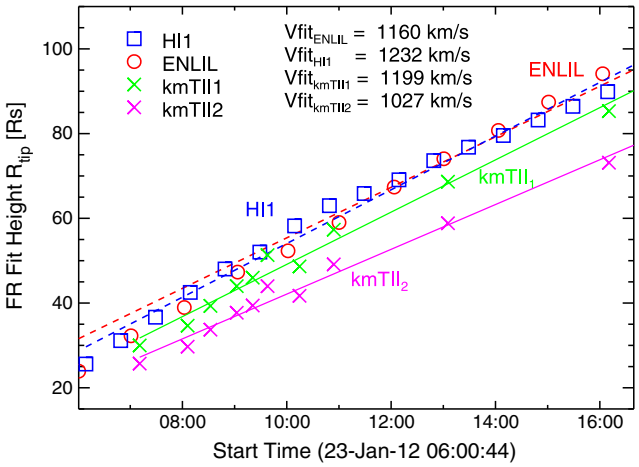

Figure 9. The time-distance profile inferred from the kmTII method, superimposed with trajectories extracted from the ENLIL model and the FR-fit to the HI1 images on 23 January 2012. Note that all the distances are measured along the CME/shock LE direction.

respectively, where n_{0enlil} = 9.7 cm^{-3} is the plasma density from the ENLIL model and n_{0avg} = 7.2 cm^{-3} is the average solar wind density at 1 AU. The results show that kmTII$_1$ has a better agreement with the ENLIL model results and the HI1 observations than kmTII$_2$. The kmTII$_1$ linear-fit shock speed is 1199 km s^{-1}, and the predicted SAT is 13:01 UT on 24 January, yielding errors of –1.6 h and 33 km s^{-1}, compared to the Wind SAT of 14:38 UT on 24 January and the FR-fit speed of 1232 km s^{-1}. The prediction errors of SAT and linear shock speed for kmTII$_2$ are ∼4 h and 205 km s^{-1}, respectively.

[21] Table 2 columns 6–8 list the ENLIL prediction errors Err$_{en}$ and the kmTII prediction errors Err$_{km1}$ and Err$_{km2}$ of kmTII$_1$ and kmTII$_2$. The mean absolute values of the prediction errors of Err$_{en}$, Err$_{km1}$, and Err$_{km2}$ are 5.8 h, 6.7 h, and 8.4 h, respectively, and their standard deviations are ±5.9, ±6.4, and ±10.4. Applying the ENLIL model density has reduced the kmTII prediction error from 8.4 to 6.7 h, yielding a mean prediction error ∼1 h larger than Err$_{en}$.

[22] Table 2 column 12 lists the measurement uncertainty in the kmTII method, which was estimated by $|d\left(\frac{R}{V_{sh}}\right)| = T_{sh}|\frac{dv}{V_{sh}}| = T_{sh}|\frac{d(1/f)}{1/f}| = T_{sh}|\frac{df}{f}|$, where R = 1 AU, V_{sh} is the shock speed (km s^{-1}) and T_{sh} is the shock travel time from the Sun to the Earth. With an average bandwidth-to-frequency ratio of $\left(|\frac{df}{f}| = \sim 20\%\right)$, the kmTII method yielded a mean uncertainty of 10.2 h.

3.3.2. Effect of CME Interaction on the kmTII Prediction

[23] Increasing observational evidences have shown that the interaction of CMEs enhances and modifies the type II radio emission. *Gopalswamy et al.* [2001b, 2002] suggested that the observed type II enhancement results from an enhanced upstream density, which reduces the Alfvén speed and increases the shock Mach number. *Vandas and Odstrcil* [2004] performed a 2.5-D MHD simulation and proposed that the enhanced magnetic fields in the flux-rope helical structure may favor acceleration of electrons by the fast-Fermi process when a fast CME/shock penetrates a slower preceding CME. *Gopalswamy* [2004] also mentioned the possible electron acceleration mechanism by reconnection between the two interacting CMEs. CME interaction can take place when CMEs originate from the same active region [*Gopalswamy et al.*, 2004] or from different active regions [*Gopalswamy et al.*, 2003]. CME interaction has been suggested to increase the travel time of CMEs to Earth [*Manoharan et al.*, 2004].

[24] When the interaction of CMEs occurs in the kmTII domain, it affects directly the kmTII prediction by changing the upstream density, the kmTII location, intensity, and bandwidth. In this section, we study two CME-CME interaction cases: the 6 September 2011 (No3) and the 7 March 2011 (No9) events in the Table 2 list. Table 3 lists the onset time, FR-fit radial speeds, half widths, propagation directions of the two interacting CMEs, and the time when the two CMEs merge together in each case. Figure 10 plots simulated 2-D density contours in the constant latitudinal plane of 25° for these two cases at 07:00 UT on 7 September and 23:01 UT on 7 March. In the figure the X axis is the Sun-Earth direction and the Y axis is the west (up)-east (down) direction. Earth is near X = 1 AU and at Y = 0 AU. The CME interaction occurred near the CME LEs for event No3, where the two CMEs originated from the same AR 11283. Figure 10 (right) shows that the plasma upstream of the shock has been replaced by the preceding CME1. The interaction interval of the two CMEs was from ∼06:00 to ∼16:00 UT on 7 September, as indicated by the spectrum (Figure 10, top left panel). In the 7 March 2011 event the two interacting CMEs originated from different ARs. The first CME$_1$ originated from AR 11166/N10E18, and the second CME$_2$ originated from AR 11164/N24W58. The interaction between the two CMEs occurred from ∼22:00 on March 7 to ∼04:00 UT on March 8. A density enhancement presented in the interaction region at the CME flanks near ∼N25W12. The maximum densities in the interaction region for these two cases are 20.7 cm^{-3} and 25.6 cm^{-3}, respectively, as shown in Figures 8b and 8c.

Table 3. Summary of the Properties of CMEs for Interacting Events[a]

CME1				CME2				
Time (UT)	Speed (km s^{-1})	Width (deg)	Direction	Time (UT)	Speed (km^{-1})	Width (deg)	Direction	Merging Time (UT)
2011/09/06 02:24	350	32	N30W07	09/06 23:05	1033	45	N20W28	09/07 15:49
2011/03/07 14:48	863	49	N21E18	03/07 20:00	2283	57	N32W58	03/07 23:10

[a]Columns 1–4: CME1 first appearance time on C2, FR-fit radial speed, face-on half width, and propagation direction to COR2 images; columns 5–8: CME2 first appearance time on C2, FR-fit radial speed, face-on width, and propagation direction to COR2 images; column 9: merging time of the two CMEs. Dates are formatted as year/month/day and month/day where applicable.

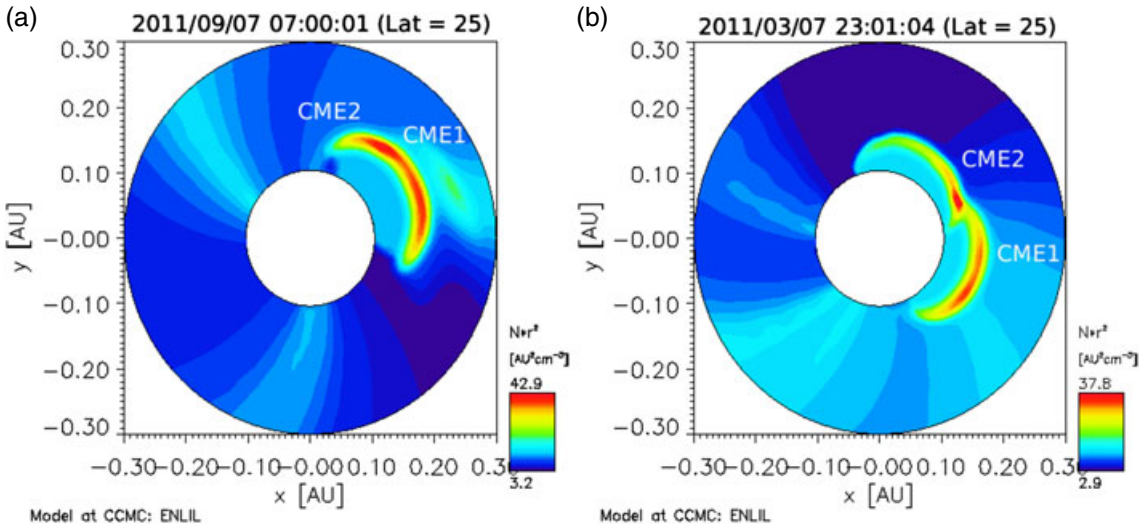

Figure 10. Simulated 2-D density contours in the constant latitude plane of 25° showing the interactions of the CMEs for events (a) No3 (6 September 2011) and (b) No9 (7 March 2011) in Table 2.

[25] Figure 11 shows (left) the dynamic spectrum detected by the Wind/Waves and (right) the kmTII time-distance profile of the shock propagation, superimposed with the shock time-distance profiles from the ENLIL model (red circle) and FR-fit to HI1 images (blue diamond) for events No3 and 9. Same as Figure 9, kmTII_1 (green cross) and kmTII_2 (magenta cross) denote the shock distances deduced from $n_{0\mathrm{enlil}}$ and $n_{0\mathrm{avg}}$, respectively. We set $n_{0\mathrm{enlil}}$ as average val-

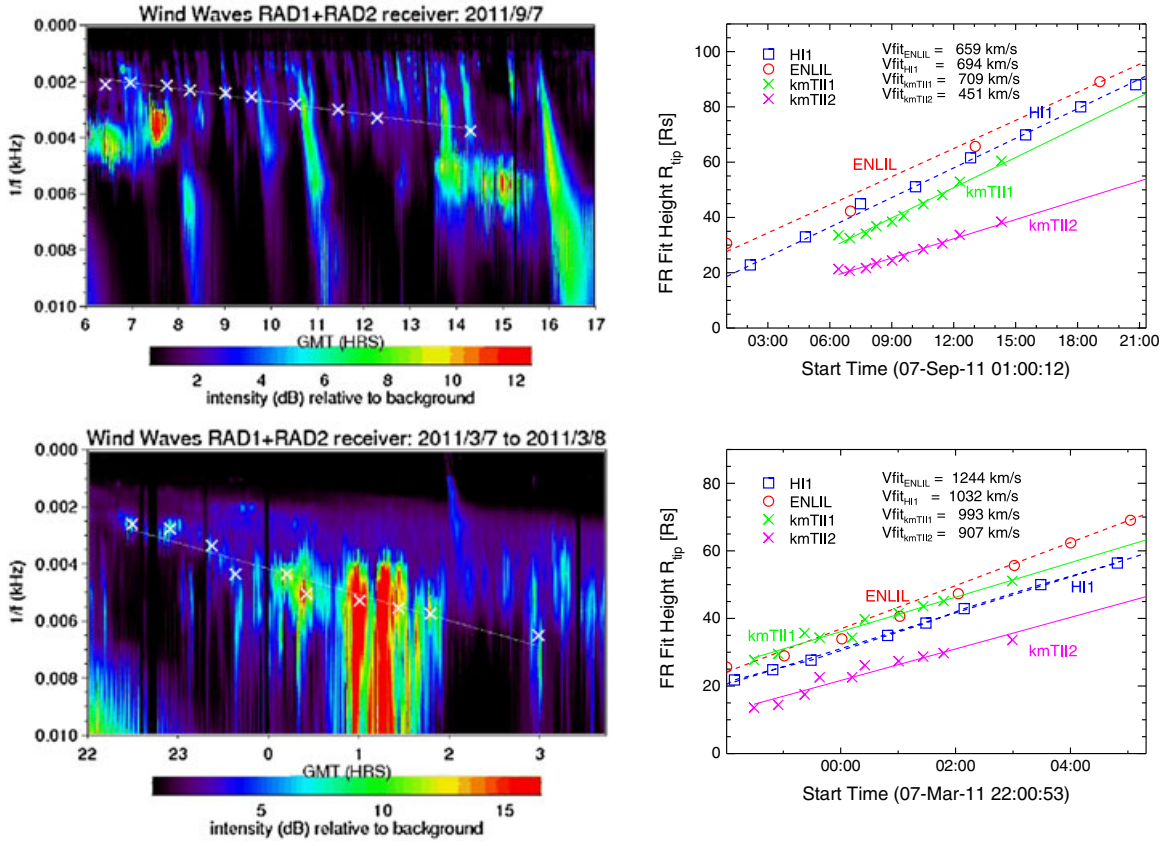

Figure 11. The kmTII dynamic spectrum detected by Wind/WAVEs on (top left) 7 September and (bottom left) 7 March 2011. Shock time-distance profile inferred from the kmTII method, superimposed with trajectories extracted from the ENLIL model and the FR-fit to HI1 images of the (top right) 6 September and (bottom right) 7 March 2011 CMEs. Note that the corresponding distances are measured along the CME interaction direction.

ues of the simulated upstream density of 17.7 cm^{-3} in No3 and 16.5 cm^{-3} in No9. In both cases, enhanced intensity patches were observed in the kmTII spectra as results of the CME interactions. In event No3, the ENLIL time-distance profile has a better agreement with the shock location as seen in HI1 observations than $kmTII_1$, while in event No9, $kmTII_1$ shows a better agreement with the observations. Both $kmTII_2$ time-distance profiles show relatively large deviations from the HI1 observations. The differences between the $kmTII_1$ and FR-fit linear shock speeds are 15 km s^{-1} and 39 km s^{-1} for the two cases, and the differences between the $kmTII_2$ and FR-fit shock speeds are 243 km s^{-1} and 125 km s^{-1}, respectively. The prediction errors of $kmTII_1$ and $kmTII_2$ are –4.9 h and 29.6 h for event No3, and 4.2 h and 10.6 h for event No9. The results show that applying the ENLIL model density improved significantly the kmTII prediction for event No3.

4. Discussion

4.1. Shock Dynamics in the Inner Heliosphere

[26] The shock speed V_s determined from the mass conservation relation [*Viñas and Scudder*, 1986] is given by

$$\mathbf{V_s} = (\rho_\mathbf{d}\mathbf{V_d} - \rho_\mathbf{u}\mathbf{V_u})/(\rho_\mathbf{d} - \rho_\mathbf{u}) \cdot \mathbf{n}$$

where **n** is the shock normal, V and ρ are the plasma speed and density, and the subscripts d and u represent the downstream and upstream values. If the shock normal and speed are both along the radial direction, the shock speed can be simplified as: $V_s = V_d + (V_d - V_u)/(r_n - 1)$, where $r_n = \rho_n/\rho_d$. For strong shocks with $r_n >> 1$, we have $V_s \simeq V_d$, i.e., the speed of driving ICME.

[27] It is well known that the dynamics of an ICME is dominated by the drag force after the driving Lorentz force vanishes beyond certain heliocentric distance [e.g., *Chen and Kunkel*, 2010; *Vršnak et al.*, 2013]. The drag acceleration resulting from the interaction of the ICME with the ambient solar wind has a quadratic form: $a = -\gamma(V - V_{sw})^2$, where $\gamma = C_d\frac{A\rho}{M}$, C_d is the drag coefficient, A and M are the ICME cross sectional area and mass, whereas ρ is the ambient solar wind density, and V and V_{sw} are the ICME speed and the ambient solar wind speed (for details, see *Cargill* [2004]). In Figure 12 we plot the shock acceleration versus the shock speed obtained from the ENLIL model output. We divided the shock propagation as two phases: (a) a fast deceleration phase at $r \leq 50R_s$ and (b) a slow deceleration phase at $r > 50R_s$. Applying quadratic curve fit to the simulation results, we get

$$\begin{cases} a_1 = -[0.0033(V_1 - 252)]^2 & 21.5 < r \leq 50R_s \\ a_2 = -[0.0022(V_2 - 361)]^2 & r > 50R_s, \end{cases} \quad (3)$$

where a_1 and a_2 are the linear-fit shock accelerations in phase 1 and phase 2, and V_1 and V_2 are the shock speed at 21.5 R_s and 50 R_s, respectively. Equation (3) corresponds to a $\gamma_1 = 0.11 \times 10^{-7}$ m^{-1} and $V_{sw1} = 252$ for phase 1 and $\gamma_2 = 0.48 \times 10^{-8}$ km^{-1} and $V_{sw2} = 361$ for phase 2. The correlation coefficients (CC) between $V_{1(2)}$ and $\sqrt{(-a_{1(2)})}$ are 0.96 and 0.95, respectively. Our simulation results suggest that the dynamics of shock follows the drag-based model in the inner heliosphere. The inferred average solar wind speeds

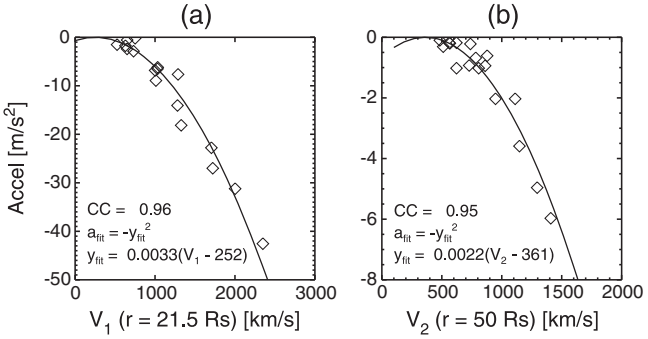

Figure 12. The shock acceleration versus the shock speed derived from the ENLIL model simulation for (a) $21.5 < r \leq 50R_s$ and (b) $r > 50R_s$.

are consistent with the solar wind model [*Sheeley et al.*, 1997]. Due to the large relative speed of $(V_{cme} - V_{sw})$ at distances closer to the Sun, the fast CME has undergone most of its deceleration within 50 R_s. From Figure 12, we can see that a_1 at $r \leq 50R_s$ is about 1 order of magnitude larger than a_2 at $r > 50R_s$. This result is consistent with our previous study of *Xie et al.* [2009], which showed that fast CME-driven shocks associated with type II bursts experienced a rapid deceleration as they propagated through the corona and then kept a nearly constant speed traveling out into the heliosphere.

[28] Using simple kinematic relations, equation (3) can serve as an empirical predictive tool for the SAT [*Gopalswamy et al.*, 2005b]. The prediction error estimation is given by $|\mathrm{dSAT}| \propto \frac{1}{V_{cme}} \times (dV_{cme}/V_{cme} - da/2V_{cme})$, where dV_{cme}, dV_{sw}, and da are deviations of the CME input speed, ambient solar wind speed, and the acceleration change due to $d(V_{cme}–V_{sw})$. Figure 13 plots dSAT as a function of dV_{cme} and dV_{sw}. Marks on each curve denote different values of CME input speeds. It is shown that dV_{cme} has larger effect on dSAT on slower CMEs than faster CMEs due to $|\mathrm{dSAT}| \propto \frac{1}{V_{cme}}$. A dV_{cme} of 500 km/s results in SAT errors of ~12 h, ~7 h, and ~5 h, respectively, for CME speeds of 1000, 1500, and 2000 km s^{-1}. Taking event No3 in our sample in Table 1 as an example, V_{FR} = 1011 km s^{-1}, V_{cone} = 914 km s^{-1}, and dV_{cme} of 196 km s^{-1} between V_{FR} and V_{cone} has resulted in a dSAT of ~6 h. Using flux-rope model speed has improved the SAT prediction from 6.87 h to 0.73 h. Comparing to the CME input speed, the solar wind speed has smaller effect on SAT. As shown in Figure 13b, a 300 km/s deviation in the solar wind speed results in around 3–6 h deviation in SAT. Thus, accurate measurements of the CME speeds are important to the ENLIL model prediction.

4.2. Improving the kmTII Prediction With ENLIL

[29] The kmTII technique is a simple empirical prediction method. The method works best when the in situ electron plasma frequency line is seen stable and when the emission drifting speed is nearly constant. The latter is usually valid at large distances from the Sun, which correspond to kilometer frequencies, because the CME has undergone most of its deceleration by that time. On the other hand, the main weakness of the technique is given by the fact that the electronic plasma density is not warranted to be stable, especially at times of high solar activity. The SAT prediction based on the average solar wind value of 7.2 cm^{-3} can have large errors

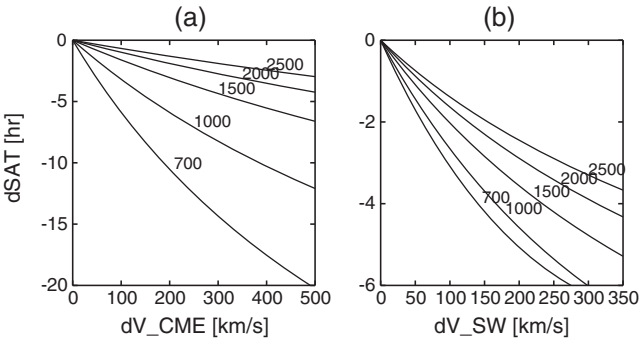

Figure 13. The SAT error as a function of errors of (a) the CME input speed and (b) the solar wind speed. Values labeled on each curve denote the CME input speed in km/s at the inner boundary at $r = 21.5R_s$.

mainly due to fluctuations in the electron plasma density during and after the detection of the radio emission.

[30] By using a better modeling of plasma density fluctuations upstream of the shock from the ENLIL model, we are able to improve the kmTII prediction. Taking the 6 September 2011 event as an example, the shock arrived at Wind at 11:46 UT on 9 September; the plasma density detected by Wind is 17.2 cm^{-3}, averaged from 09:40 to 11:40 UT. This unusually high plasma density resulted from the interaction of two CMEs, as shown in Figure 10a. The preceding CME has replaced the upstream plasma ahead of the shock associated with the later CME. The ENLIL model output n_0 = 17.7 cm^{-3} agreed well with the in situ actual measurement of the plasma density from Wind. Due to large discrepancy between n_0 and the average solar wind density, the kmTII prediction using n_0 = 7.2 cm^{-3} caused a large SAT error of 29.6 h. Using the ENLIL output has significantly reduced the SAT prediction error from 29.6 h to –4.9 h. In addition, the shock distances $kmTII_1$ inferred from equation (1) by taking n_0 = 17.7 cm^{-3} matches better with the HI1 observations than $kmTII_2$ using n_0 = 7.2 cm^{-3}, as shown in Figure 11. The good agreement between the $kmTII_1$ points and the HI1 points has in turn served as a validation for the ENLIL model results.

[31] On the other hand, the kmTII method assumed that the type II emission is originated in a parcel that is traveling along the Sun-Earth line, which most of the time is not exactly the case, as we know that the type II radio bursts tend to occur at the shock nose and/or interaction regions, where the shock intensity has been enhanced. For instance, for the 23 January 2012 event, the shock nose direction is N33W21 (∼38° away from the Sun-Earth line direction) where the CME/shock has encountered a dense streamer. The radio emission that occurred at the LE has resulted in a faster $kmTII_1$ shock speed of 1199 km/s (Figure 9) compared to the shock flank speed of 982 km/s along the Sun-Earth direction (Figure 5b). Also, due to the deceleration of the shock speed, the $kmTII_1$ shock speed detected at earlier emission time was close to the average shock transit speed (1183 km/s) but much faster than the Wind shock speed of 625 km/s. Thus, a limitation of the kmTII technique is that it cannot predict the detailed shock dynamics, but only the average features of the shock.

5. Conclusion

[32] We have studied the isolated and synergistic performance of two methods of predicting IP shock location and strength throughout the inner heliosphere: (1) the ENLIL simulation and (2) the kmTII prediction. To evaluate the ENLIL method, we applied two sets of input parameters from the cone-model fitting and flux-rope model fitting to the ENLIL model for 16 Earth-directed CMEs. By comparing the simulation results from the two sets of inputs, we examined how the model performance depends on the CME input speed. We found that by using the FR-fit CME speed, the ENLIL model provided a better SAT prediction, the mean prediction errors for the FR-fit and cone-fit inputs being 4.90 ± 5.92 h and 5.48 ± 6.11 h, respectively. A deviation of 100 km s^{-1} from the actual CME speed has resulted in a SAT prediction error of 3.46 h on average. In addition, our ENLIL simulation results confirm that in the inner heliosphere with $R > 21.5Rs$, the shock dynamics agrees with the drag-based model [*Cargill*, 2004; *Vršnak et al.*, 2013]. The drag force has a quadratic form and is proportional to the square of the relative speed between CME and solar wind. The shock deceleration can be divided into two phases: (1) a fast deceleration phase with $r \leq 50R_s$ and (2) a slow deceleration phase with $r > 50R_s$. The average deceleration within $50R_s$ is about 1 order of magnitude larger than that beyond $50R_s$.

[33] The ENLIL model predicted not only the kinematics of shock evolution well but also reproduced the time-dependent ambient and/or transient features of the solar wind structures. Since electron plasma density upstream of shocks is a key factor to the kmTII method, it is intended to improve the kmTII technique by combining it with the ENLIL density output. After testing this synergistic approach, we found that by taking into account the effect of fluctuating solar wind density, the SAT prediction of the kmTII technique was largely improved. The mean prediction errors of kmTII using (1) the ENLIL model density, n_{0enlil}, and (2) the average solar wind plasma density, n_{0avg} = 7.2 cm^{-3}, are 6.7 ± 6.4 h and 8.4 ± 10.4 h, respectively. Applying the ENLIL density has improved the mean kmTII prediction error by ∼2 h and the standard deviation by 4.0 h.

[34] By reproducing well the time-dependent structure and physics of ambient and transient features, the ENLIL model is also capable of accurately simulating CME-CME and CME-streamer interactions. These interactions alter significantly the plasma density upstream of shocks and directly affect kmTII predictions. Therefore, we have studied in depth the two interaction events present in our sample, i.e., events No3 and No9 in Table 2. For these events, combining kmTII with the ENLIL model density has drastically reduced the SAT prediction error from 29.6 h to –4.9 h for No3 and 10.6 h to 4.2 h for No9. The kmTII method using n_{0enlil} yielded a more accurate time-distance and speed profiles of the shock than using n_{0avg}. As shown in Figure 11, the shock time-distance profiles inferred from $kmTII_1$ showed a better agreement with the HI1 observations of CME/shock locations than $kmTII_2$. Furthermore, the combination of results derived from the kmTII method and the ENLIL simulation, together with white-light data, provide insight into IP shock formation location and strength, as well as important implications for SEP acceleration.

[35] Finally, note that the ENLIL model requires the CME density and temperature as input at 0.1 AU which are not directly derived from the observations; this brings in a degree of uncertainty. The uncertainty in the CME density and temperature results in a variation in shock arrival time of ∼7 h [*Xie et al.*, 2012]. In Table 1 there are four slow CMEs with $V_{FR} < 510\,km\,s^{-1}$ having much larger prediction errors than those events with $V_{FR} > 510\,km\,s^{-1}$. The mean Err_F and Err_c for these four CMEs are 10.2 h and 9.42 h. We found that when selecting dcld = 2 (density enhancement factor of cloud to fast solar wind) rather than default dcld of 4 in the simulations, the mean Err_F reduced from 10.2 h to 5.82 h, and the mean Err_c reduced from 9.42 h to 5.83 h. This suggests that the slow CMEs may have less mass than the fast CMEs and have encountered more effective drag forces during their propagation from the Sun to the Earth [*Cargill*, 2004]. Using coronagraph observations combining the radio data, it is likely to provide a better constraint on the density input for the ENLIL model and thus improve the model performance. Further investigation will be conducted in future work.

[36] **Acknowledgments.** The authors would like to thank the support of the STEREO, SOHO, WIND, and ACE teams. The STEREO SECCHI data are produced by a consortium of RAL (UK), NRL (USA), LMSAL (USA), GSFC (USA), MPS (Germany), CSL (Belgium), IOTA (France), and IAS (France). The SOHO LASCO data are produced by a consortium of the Naval Research Laboratory (USA), Max-Planck-Institut für Aeronomie (Germany), Laboratoire d'Astronomie (France), and the University of Birmingham (UK). We acknowledge magnetogram data from NSO/GONG (Global Oscillation Network Group) and the WIND data from NASA's Space Physics Data Facility. This work was supported by NASA LWS TR&T program (08-LWSTRT08-0029). H.C. is a member of Carrera del Investigador Científico, CONICET.

[37] Philippa Browning thanks the reviewers for their assistance in evaluating this paper.

References

Aguilar-Rodriguez, E., N. Gopalswamy, R. MacDowall, S. Yashiro, and M. L. Kaiser (2005), A universal characteristic of type II radio bursts, *J. Geophys. Res.*, *110*, A12S08, doi:10.1029/2005JA011171.

Arge, C. N., and V. J. Pizzo (2000), Improvement in the prediction of solar wind conditions using near-real time solar magnetic field updates, *J. Geophys. Res.*, *105*, 10,465–10,480.

Arge, C. N., J. G. Luhmann, D. Odstrcil, C. J. Schrijver, and Y. Li (2004), Stream structure and coronal sources of the solar wind during the may 12th, 1997 CME, *J. Atmos. Sol. Terr. Phys.*, *66*, 1295–1309.

Bougeret, J.-L., et al. (1995), Waves: The radio and plasma wave investigation on the Wind spacecraft, *Space Sci. Rev.*, *71*, 231–263, doi:10.1007/BF00751331.

Brueckner, G. E., et al. (1995), The Large Angle Spectroscopic Coronagraph (LASCO), *Sol. Phys.*, *162*, 357–402, doi:10.1007/BF00733434.

Cargill, P. J. (2004), On the aerodynamic drag force acting on interplanetary coronal mass ejections, *Sol. Phys.*, *221*, 135–149, doi:10.1023/B:SOLA.000003336610725.a2.

Chen, J., and V. Kunkel (2010), Temporal and physical connection between coronal mass ejections and flares, *Astrophys. J.*, *717*, 1105–1122, doi:10.1088/0004-637X/717/2/1105.

Cremades, H., O. St.Cyr, and M. Kaiser (2007), A tool to improve space weather forecasts: Kilometric radio emissions from Wind/WAVES, *Space Weather*, *5*, S08001, doi:10.1029/2007SW000314.

Domingo, V., B. Fleck, and A. I. Poland (1995), SOHO: The Solar and Heliospheric Observatory, *Space Sci. Rev.*, *72*, 81–84, doi:10.1007/BF00768758.

Eyles, C. J., et al. (2009), The heliospheric imagers onboard the STEREO Mission, *Sol. Phys.*, *254*, 387–445, doi:10.1007/s11207-008-9299-0.

Gopalswamy, N. (2004), Recent advances in the long-wavelength radio physics of the Sun, *Planet. Space Sci.*, *52*, 1399–1413, doi:10.1016/j.pss.2004.09.016.

Gopalswamy, N. (2011), Coronal mass ejections and solar radio emissions, *Planet. Sol. Heliospheric Radio Emiss. (PRE VII)*, pp. 325–342.

Gopalswamy, N., S. Yashiro, M. L. Kaiser, R. A. Howard, and J.-L. Bougeret (2001a), Characteristics of coronal mass ejections associated with long-wavelength type II radio bursts, *J. Geophys. Res.*, *106*, 29,219–29,230, doi:10.1029/2001JA000234.

Gopalswamy, N., S. Yashiro, M. L. Kaiser, R. A. Howard, and J.-L. Bougeret (2001b), Radio signatures of coronal mass ejection interaction: Coronal mass ejection cannibalism?, *Astrophys. J.*, *548*, L91–L94, doi:10.1086/318939.

Gopalswamy, N., S. Yashiro, G. Michalek, M. L. Kaiser, R. A. Howard, D. V. Reames, R. Leske, and T. von Rosenvinge (2002), Interacting coronal mass ejections and solar energetic particles, *Astrophys. J.*, *572*, L103–L107, doi:10.1086/341601.

Gopalswamy, N., S. Yashiro, A. Lara, M. L. Kaiser, B. J. Thompson, P. T. Gallagher, and R. A. Howard (2003), Large solar energetic particle events of cycle 23: A global view, *Geophys. Res. Lett.*, *30*, 8015, doi:10.1029/2002GL016435.

Gopalswamy, N., S. Yashiro, S. Krucker, G. Stenborg, and R. A. Howard (2004), Intensity variation of large solar energetic particle events associated with coronal mass ejections, *J. Geophys. Res.*, *109*, A12105, doi:10.1029/2004JA010602.

Gopalswamy, N., E. Aguilar-Rodriguez, S. Yashiro, S. Nunes, M. L. Kaiser, and R. A. Howard (2005a), Type II radio bursts and energetic solar eruptions, *J. Geophys. Res.*, *110*, A12S07, doi:10.1029/2005JA011158.

Gopalswamy, N., A. Lara, P. K. Manoharan, and R. A. Howard (2005b), An empirical model to predict the 1-AU arrival of interplanetary shocks, *Adv. Space Res.*, *36*, 2289–2294, doi:10.1016/j.asr.2004.07.014.

Gopalswamy, N., S. Yashiro, G. Michalek, H. Xie, P. Mäkelä, A. Vourlidas, and R. A. Howard (2010), A catalog of halo coronal mass ejections from SOHO, *Sun and Geosphere*, *5*, 7–16.

Joshi, N. C., et al. (2013), Multi- Q5 wavelength study of eruptive events on January 23, 2012 associated with a major solar energetic particle event, *Adv. Space Res.*, *52*(1), 1–14, doi:10.1016/j.asr.2013.03.009.

Kaiser, M. L., T. A. Kucera, J. M. Davila, O. C. S. Cyr, M. Guhathakurta, and E. Christian (2008), The STEREO Mission: An introduction, *Space Sci. Rev.*, *136*, 5–16.

Leblanc, Y, G. A. Dulk, and J.-L. Bougeret (1998), Tracing the electron density from the corona to 1 AU, *Sol. Phys.*, *183*, 165–180.

Manoharan, P. K., N. Gopalswamy, S. Yashiro, A. Lara, G. Michalek, and R. A. Howard (2004), Influence of coronal mass ejection interaction on propagation of interplanetary shocks, *J. Geophys. Res.*, *109*, A06109, doi:10.1029/2003JA010300.

Mewaldt, R. A. (2006), Solar energetic particle composition, energy spectra, and space weather, *Space Sci. Rev.*, *124*, 303–316, doi:10.1007/s11214-006-9091-0.

Odstrcil, D., and V. J. Pizzo (2009), Numerical heliospheric simulations as assisting tool for interpretation of observations by STEREO heliospheric imagers, *Sol. Phys.*, *259*, 297–309, doi:10.1007/s11207-009-9449-z.

Odstrcil, D., P. Riley, and X. P. Zhao (2004), Numerical simulation of the 12 May 1997 interplanetary CME event, *J. Geophys. Res.*, *109*, A02116, doi:10.1029/2003JA010135.

Odstrcil, D., V. Pizzo, and C. N. Arge (2005), Propagation of the 12 May 1997 interplanetary coronal mass ejection in evolving solar wind structures, *J. Geophys. Res.*, *110*, A02106, doi:10.1029/2004JA010,745.

Reiner, M. J., M. L. Kaiser, J. Fainberg, and R. G. Stone (1998), A new method for studying remote type II radio emissions from coronal mass ejection-driven shocks, *J. Geophys. Res.*, *103*, 29,651–29,664.

Sheeley, N. R., Jr., et al. (1997), Measurements of flow speeds in the corona between 2 and 30 R sub sun, *Astrophys. J.*, *484*, 472, doi:10.1086/304338.

Thernisien, A. F. R., R. A. Howard, and A. Vourlidas (2006), Modeling of flux rope coronal mass ejections, *Astrophys. J.*, *652*, 763–773.

Toth, G., and D. Odstrcil (1996), Comparison of some flux corrected transport and total variation diminishing numerical schemes for hydrodynamic and magnetohydrodynamic problems, *J. Comput. Phys.*, *128*, 82–100.

Tsurutani, B. T., E. J. Smith, W. D. Gonzalez, F. Tang, and S. I. Akasofu (1988), Origin of interplanetary southward magnetic fields responsible for major magnetic storms near solar maximum (1978–1979), *J. Geophys. Res.*, *93*, 8519–8531, doi:10.1029/JA093iA08p08519.

Vandas, M., and D. Odstrcil (2004), Acceleration of electrons by interacting CMEs, *Astron. Astrophys.*, *415*, 755–761, doi:10.1051/0004-6361:20031763.

Viñas, A. F., and M. P. Holland (2005), Shock and Discontinuities Analysis Tool (SDAT). Abstracts: p. B10 presented at AGU Spring Meeting.

Viñas, A. F., and J. D. Scudder (1986), Fast and optimal solution to the 'Rankine-Hugoniot problem', *J. Geophys. Res.*, *91*, 39–58, doi:10.1029/JA091iA01p00039.

Vršnak, B., et al. (2013), Propagation of interplanetary coronal mass ejections: The drag-based model, *Sol. Phys.*, *285*, 295–315, doi:10.1007/s11207-012-0035-4.

Xie, H., L. Ofman, and G. Lawrence (2004), Cone model for halo CMEs: Application to space weather forecasting, *J. Geophys. Res.*, *109*, A03109, doi:10.1029/2003JA010,226.

Xie, H., N. Gopalswamy, and O. C. S. Cyr (2009), Modeling and prediction of fast CME/shocks associated with type II bursts, in *IAU Symposium, IAU Symposium*, pp. 489–491, doi:10.1017/S1743921309029755.

Xie, H., D. Odstrcil, L. Mays, O. C. St. Cyr, N. Gopalswamy, and H. Cremades (2012), Understanding shock dynamics in the inner heliosphere with modeling and Type II radio data: The 2010-04-03 event, *J. Geophys. Res.*, *117*, A04105, doi:10.1029/2011JA017304.